Temporal Variability of the Energy Balance of Thick Arctic Pack Ice

R. W. LINDSAY

Polar Science Center, Applied Physics Laboratory, College of Ocean and Fishery Sciences, University of Washington, Seattle, Washington

(Manuscript received 17 December 1996, in final form 20 June 1997)

ABSTRACT

The temporal variability of the six terms of the energy balance equation for a slab of ice 3 m thick is calculated based on 45 yr of surface meteorological observations from the drifting ice stations of the former Soviet Union. The equation includes net radiation, sensible heat flux, latent heat flux, bottom heat flux, heat storage, and energy available for melting. The energy balance is determined with a time-dependent 10-layer thermodynamic model of the ice slab that determines the surface temperature and the ice temperature profile using 3-h forcing values. The observations used for the forcing values are the 2-m air temperature, relative humidity and wind speed, the cloud fraction, the snow depth and density, and the albedo of the nonponded ice. The downwelling radiative fluxes are estimated with parameterizations based on the cloud cover, the air temperature and humidity, and the solar angle. The linear relationship between the air temperature and both the cloud fraction and the wind speed is also determined for each month of the year.

The annual cycles of the mean values of the terms of the energy balance equation are all nearly equal to those calculated by others based on mean climatological forcing values. The short-term variability, from 3 h to 16 days, of both the forcings and the fluxes, is investigated on a seasonal basis with the discreet wavelet transform. Significant diurnal cycles are found in the net radiation, storage, and melt, but not in the sensible or latent heat fluxes. The total annual ice-melt averages 0.67 m, ranges between 0.29 and 1.09 m, and exhibits large variations from year to year. It is closely correlated with the albedo and, to a lesser extent, with the latitude and the length of the melt season.

1. Introduction

The surface energy balance is an essential element of the climate in any region of the world, but it takes on added significance in the polar regions, where small changes in the surface energy balance can lead to dramatic changes in the surface itself. The response of the ice to climatic-averaged forcing conditions has been modeled in the past, but the variability of the forcing parameters and the variability of the ice's response have not. The focus of this study is to determine the variability of the forcing parameters and the energy fluxes on temporal scales that include short-term variability from hours to days, seasonal variability, and interannual variability. A time-dependent thermodynamic model of the ice is used to estimate the energy balance, and surface meteorological observations are used to provide the forcings. The observations are from an extensive dataset from the North Pole (NP) drifting ice camps of the former Soviet Union. The calculations are based on 45 station-years of 3-h observations beginning in 1957 and ending in 1990.

Consider the energy balance of a slab of ice. The fluxes of energy to the ice are the net radiation F_r of the ice slab, the sensible heat flux at the surface F_s, the latent heat flux at the surface F_q, and the conductive heat flux at the bottom of the ice F_b. The balance is then expressed as a sum of the fluxes at the top and bottom surfaces minus the energy stored in the ice S and the energy available for melting ice M.

$$F_r + F_s + F_q + F_b - S - M = 0. \qquad (1)$$

All fluxes are considered positive if directed toward the ice. The six terms of this equation are the principal focus of this study.

The surface energy balance determines the surface temperature and the sign and magnitude of the sensible heat flux to the ice from the atmosphere. The heat flux in the lower atmosphere (along with the wind stress) helps to establish the depth and the structure of the atmospheric boundary layer and hence the efficiency of the coupling between the atmosphere and the ice (Overland and Davidson 1992). The energy balance at the bottom of the ice helps to fix the freezing rate and the brine rejection rate and hence the evolution of the oceanic mixed layer. Thus, the energy balance of the ice determines the structure and evolution of the ice, the

Corresponding author address: R. W. Lindsay, Polar Science Center, Applied Physics Laboratory, 1013 NE 40th Street, Seattle, WA 98105.
E-mail: lindsay@apl.washington.edu

atmosphere, and the ocean and the dynamic coupling between the three of them.

The first calculation of the thermal evolution of the ice over the entire annual cycle was performed by Maykut and Untersteiner (1971, hereafter MU71). They used climatological values for the downwelling radiative fluxes, the sensible and latent heat fluxes, and the albedo and snow depth. They integrated the model over many annual cycles until an equilibrium ice thickness was obtained. The study reported here is very much in the tradition of the MU71 study, with the important addition of the use of 3-h observations for forcings and the calculation of 45 distinct annual cycles.

An additional study by Maykut (1982, hereafter M82) extended the MU71 study to different ice-thickness classes and to a determination of the annual cycle of the regional heat balance in the Beaufort Sea. He also calculated the annual cycle for 3-m-thick ice, again using climatological forcing values. The current study obtains results roughly similar to his for the mean values of the terms in (1) and adds information about the temporal variability. A somewhat more complex thermodynamic model of sea ice is that of Ebert and Curry (1993). They include different ice types, a complex parameterization of the albedo, melt-pond coverage and drainage, and a prescribed deformation rate. They use this model to investigate ice/albedo feedback mechanisms. An extensive study by Makshtas (1991) of the winter heat balance of the Arctic ice also uses a thermodynamic model.

This paper is organized as follows: section 2 describes the drifting ice-station data, the energy balance model, and sample results for a single station and year. Section 3a summarizes the results for all 45 station years and highlights the annual cycle and the seasonal variability of the various terms of the energy balance equation. Section 3b then summarizes the variability of the terms at temporal scales from 3 h to 16 days for each of the four seasons, and section 3c assesses the interannual and spatial variability, again on a seasonal basis. Comments and conclusions are given in section 4.

2. Surface energy balance model

a. Model forcing parameters

The series of drifting ice stations operated by the former Soviet Union provides a unique and remarkable set of meteorological observations from the interior of the Arctic ice pack. The entire set of surface meteorological data has recently been made available to the west through the cooperation of the Arctic and Antarctic Research Institute (AARI) in Leningrad. The data are available on a CD-ROM from the National Snow and Ice Data Center (NSIDC 1996). The first station in the series was established in 1937 and operated for less than a year. The second was established in 1950 and operated for 1 yr. Beginning in 1954, there was continuous coverage by at least one station, usually two, until the end of the program in 1991 with the closing of NP-31. The station with the longest continuous record is NP-22, which remained active for over 8 yr. There are 196 321 observations on the CD-ROM providing approximately 73 station years of data.

In addition to the standard meteorological variables, some of the stations also reported various radiative fluxes including downwelling direct, diffuse, and global shortwave radiation, net radiation (long and shortwave), and albedo. Summaries of these observations are available in a recently translated report (Marshunova and Mishin 1994). The average daily values for stations NP-17–NP-31 are also available on the NSIDC CD-ROM.

The model-forcing parameters derived from the NP drifting ice-station dataset include the air temperature, the mixing ratio, the wind speed, the air pressure, the downwelling short- and longwave radiative fluxes, the snow depth and density, and the surface albedo. Monthly mean forcing parameters are used when missing values are encountered. For convenience, 45 complete calendar years, January–December, were selected for computing the energy balance. This represents 67% of the entire dataset. Figure 1 shows the mean monthly positions of the stations used in this study. The stations are concentrated in the central Arctic basin, with relatively few in the peripheral seas. The stations extend from NP-6 through NP-31 and span the years 1957–90. In some years, as many as three stations reported simultaneously.

The air temperature was measured in standard meteorological observing screens at a height of 2 m. The winds were measured at various heights ranging from 2 to 10 m. All of the wind measurements were corrected to a height of 2 m assuming a logarithmic wind profile and a roughness length of $z_0 = 1.3$ mm. The mixing ratio was determined from the reported relative humidity (with respect to liquid water) and the reported air temperature.

The albedo of the surface is the monthly averaged albedo for each station and year. These values are reported by Marshunova and Mishin (1994) and represent observations of the nonponded surface near the meteorological observing site. The reported albedo is averaged over the entire month and represents the albedo for the average cloud cover for the month. Hence, no additional adjustment is made to the albedo for day-to-day changes in the cloud cover. There is considerable variability in the monthly albedo values from station to station and from year to year; for example, the values in April range from 0.74 to 0.89 and those in July from 0.45 to 0.80. The high values in July represent years, when not all of the snow melted in the vicinity of the meteorological observing site or when summer snowfalls occurred. The monthly averaged albedo values may significantly smooth abrupt transitions in the spring and fall. The albedo is the most

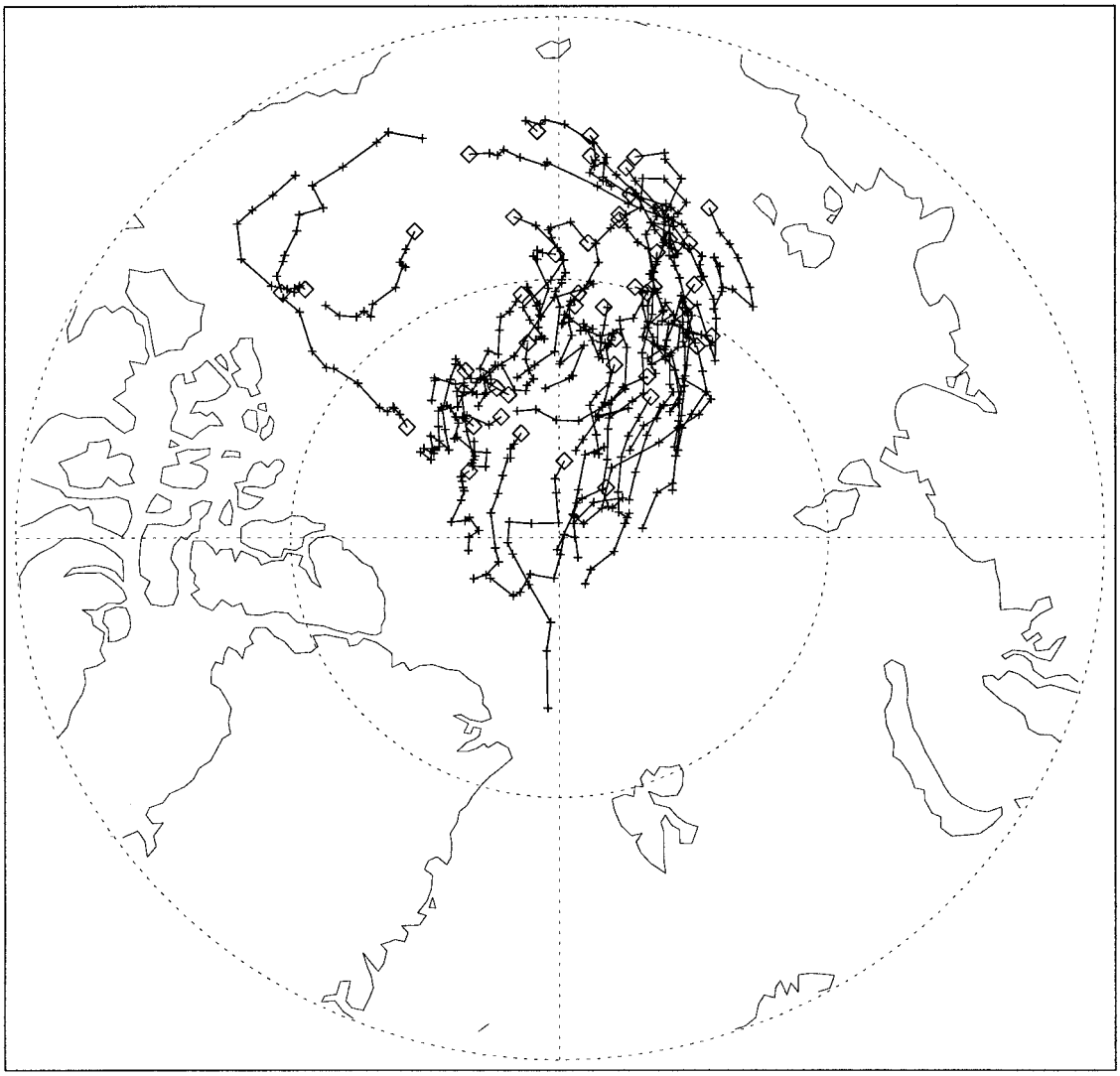

FIG. 1. Map of the mean monthly positions of the NP drifting ice stations used in this study. The locations of the stations during each of the 45 annual cycles are connected by separate lines, with January enclosed in a box.

significant and perhaps the least well measured of the forcing parameters. It must be stressed that the values we use do not include ponds, thin ice, or leads, and thus the computed energy balance cannot be generalized to all thick ice or to the ice cover as a whole. Yet, the calculations do represent a significant portion of the ice cover and characterize the energy exchange particularly well when the surface is frozen.

The snow depth and snow density are taken from the values measured at stakes near the weather observing sites. This dataset was also made available through a cooperative agreement with AARI and is on the NSIDC (1996) CD-ROM. The data we used here consist of blended 5-day values of the snow depth and density based on both daily values measured at snow stakes and more sporadic measurements obtained from 1-km-long snow-measurement lines (I. Rigor 1996, personal communication).

The radiative fluxes for this study are estimated using parameterizations involving the solar zenith angle, reported cloud cover, surface albedo, air temperature, and humidity. We use parameterizations of the radiative fluxes, not the measured values, because the NSIDC CD-ROM includes only the daily average downwelling shortwave flux values (not 3-h observations), and the downwelling longwave radiation is available only in the winter. The parameterized downwelling long- and shortwave fluxes are determined with procedures recommended by Key et al. (1996) who compared several different parameterization schemes with measured fluxes obtained over several weeks in the spring of 1993 at Resolute, Northwest Territories,

Canada, and over an annual cycle at Barrow, Alaska. For downwelling shortwave fluxes, they recommend the following parameterization by Shine (1984):

$$F_{\text{sw,clr}} = \frac{S_0 \cos^2 Z}{1.2 \cos Z + 0.001(1 + \cos Z)e + 0.0455} \quad (2)$$

$$F_{\text{sw,cld}} = \frac{(53.5 + 1274.5 \cos Z) \cos^{0.5} Z}{1 + 0.139(1 - 0.9345\alpha)\tau} \quad (3)$$

$$F_{\text{dsw}} = (1 - c)F_{\text{sw,clr}} + cF_{\text{sw,cld}}, \quad (4)$$

in which $F_{\text{sw,clr}}$, $F_{\text{sw,cld}}$, and F_{dsw} are the downwelling shortwave radiative fluxes for clear skies, cloudy skies, and all skies. Other parameters are the solar zenith angle Z, the solar constant S_0, the near-surface vapor pressure e, the surface albedo α, the cloud optical depth τ, and the cloud fraction c. The albedo in (3) represents effects of multiple cloud-to-ground reflections and should be the average albedo of a wide area around the observation site. For the purposes of the flux parameterization, the albedo in the months of July and August is reduced by 0.05 to account for melt ponds and leads in the vicinity of the station which would reduce the amount of multiple reflections between the clouds and the ice. This value of α used for the reduction is an additional source of uncertainty in the downwelling shortwave flux estimation.

The average daily global shortwave flux measured at stations dating back to NP-17 is used to validate the downwelling fluxes. Based on comparison between the parameterized and observed shortwave fluxes, a cloud optical depth was chosen for each month to minimize the mean monthly difference between them. In the spring and fall it was not possible to find a cloud optical depth that would entirely remove the bias, so a value of 1.0 was assumed. This inability may be due to the difficulties in comparing averaged daily values when the sun is above the horizon for only a small part of the day as well as to possible errors in the parameterization scheme or in the measurements at very low sun angles. The optical depths used for March–September are 1.0, 1.0, 3.5, 5.3, 6.8, 6.2, and 1.0. Figure 2a compares the downwelling shortwave parameterization for daily averaged values with the measured global shortwave radiative flux. For days in which the flux is greater than 10 W m^{-2} (N = 6228), the parameterized fluxes average 0.4 W m^{-2} less than the measured fluxes, and the rms difference is 31.7 W m^{-2}. The monthly bias ranges from -7.0 W m^{-2} in April to 4.7 W m^{-2} in June. If a constant value of 8 is used for the cloud optical depth, as done by Key et al. (1996), the parameterized fluxes average 10.6 W m^{-2} less than the measured fluxes.

For downwelling longwave fluxes F_{dlw}, Key et al. (1996) recommend the Efimova (1961) parameterization of the clear-sky flux used in the Jacobs (1978) parameterization for all skies:

$$\mathrm{F}_{\text{dlw}} = \sigma T^4(0.746 + 0.0066e)(1 + 0.26c), \quad (5)$$

where σ is the Boltzman constant and T is the near-surface air temperature. Figure 2b compares the daily averaged values during winter. Measured longwave fluxes at the NP stations are unavailable once the sun comes up. During the dark time of the year, the parameterized fluxes average 1.5 W m^{-2} less than the measured fluxes, with an rms difference of 11.9 W m^{-2} (N = 4403).

The errors associated with these parameterized radiative fluxes are comparable to the best estimates of the downwelling surface radiative fluxes made from satellites. Schweiger and Key (1997) used a neural net-based technique to retrieve the surface fluxes from TOVS radiances; they report that in their test cases (79 days from drifting ice stations and 180 days from a coastal station) the daily averaged fluxes show rms errors of 35 W m^{-2} for the downwelling shortwave fluxes and 20 W m^{-2} for the downwelling longwave fluxes. The mean measurement errors in their study were less than 4 W m^{-2}.

b. Model description

The time-varying components of the surface energy balance (1) are computed using a thermodynamic ice model. As mentioned previously, the forcing parameters derived from observations include the air temperature, the mixing ratio, the wind speed, the air pressure, the downwelling short- and longwave radiative fluxes, the snow depth and density, and the surface albedo. The important free parameters are the surface (skin) temperature, the ice-temperature profile, and the surface fluxes. The ice thickness is held constant at 3.0 m. The use of a constant ice thickness is justified, because changes in the thickness of multiyear ice during the year do not greatly modify the surface fluxes. The focus of this study is the variability of the surface fluxes for ice of a fixed thickness, and to change the ice thickness with time would add a confusing variable. In addition, the forcing parameters used in the model are not strong functions of the ice thickness if the ice is a multiyear floe and the ice stations were established on floes of different thicknesses. The 3-m ice thickness is near the equilibrium ice thickness of 2.88 m found by MU71.

The model has ten levels, seven within the ice and three within the snow. The levels are quadratically spaced in the ice and snow separately to give thinner layers near the surface. The snow layers are spaced in proportion to the snow depth. When the snow is deep (about 40 cm), the top snow layer is 4 cm thick. The layer thicknesses are consistent with the recommendations of Guest and Davidson (1994) who find that in new snow fluctuations in the surface forcing at a scale of 3 h penetrate about 5 cm deep. The top ice layer is 7 cm thick. The models for the surface energy balance and the subsurface temperature profile have been adapted from portions of the Community Climate Model Version 2 (CCM2) developed by the National Center for Atmospheric Research (Hack et al. 1993). The ice-temperature profile is calculated by solving the thermal dif-

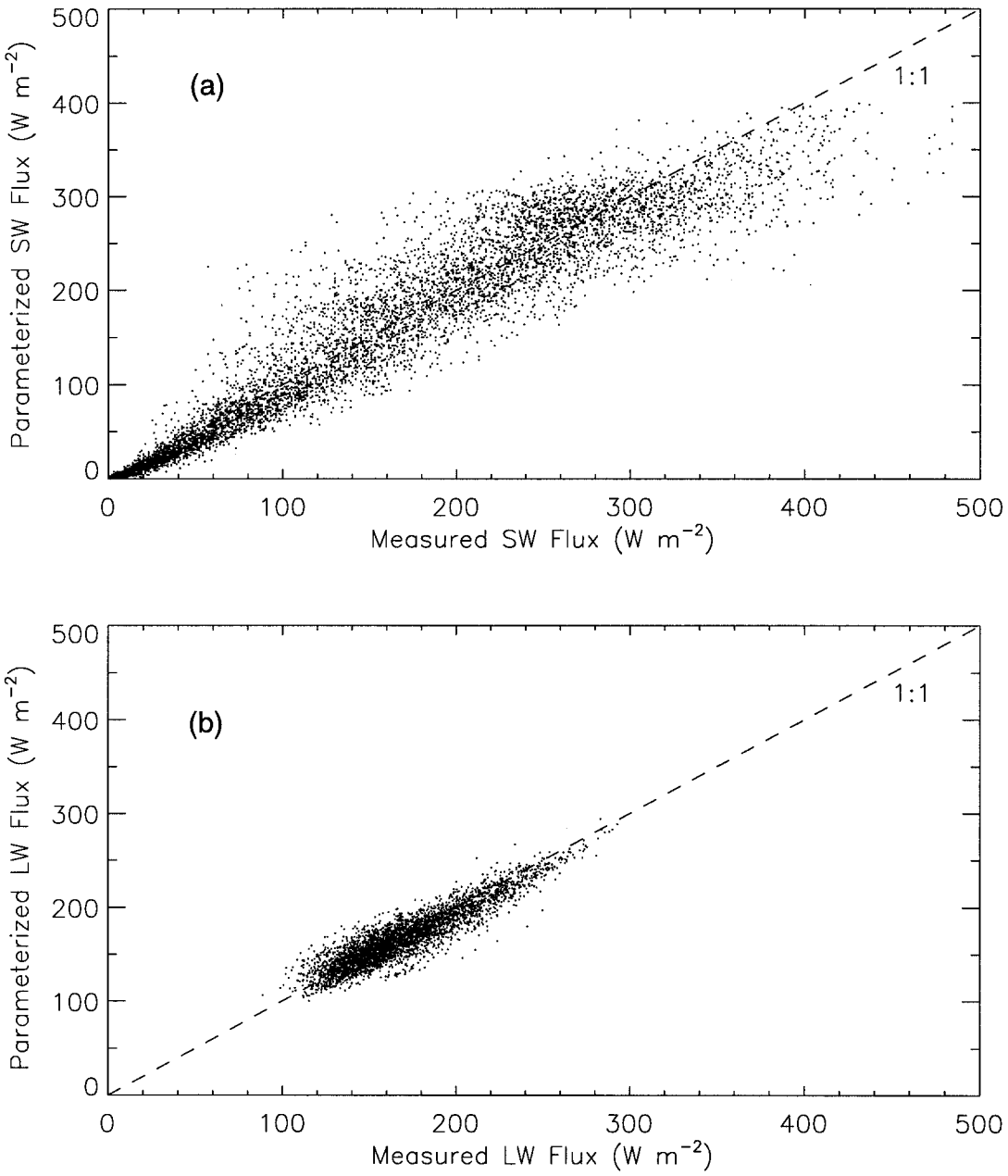

FIG. 2. Comparison of parameterized and measured daily average downwelling radiative fluxes: (a) shortwave (6228 days), and (b) longwave, during the winter only (4403 days).

fusivity equation with a fully implicit Crank–Nicholson scheme. The model integrates forward in time with a time step of $\Delta t = 3$ h.

An energy balance equation is applied to each layer i; $i = 1$ at the surface to $i = 10$ at the bottom. For any layer, the energy balance is

$$(F_{r,i} - F_{r,i+1}) + F_s + F_q + (F_{c,i} - F_{c,i+1}) - S_i - M_i = 0, \quad (6)$$

where $F_{r,i}$ is the radiative flux at the top of the layer, F_s and F_q are the turbulent fluxes (zero except at the surface), $F_{c,i}$ is the conductive flux at the bottom of the layer, and S_i and M_i are the heat storage and energy available for melting within the layer. We will treat each of the terms in turn.

The net radiation at the surface is

$$F_r = F_{r,1} = (1 - \alpha)F_{\text{dsw}} + \varepsilon(F_{\text{dlw}} - \sigma T_{\text{sfc}}^4), \quad (7)$$

where F_{dsw} and F_{dlw} are the downwelling shortwave and longwave fluxes at the surface, α is the albedo of the ice, ε is the surface emissivity, σ is the Boltzman constant,

and $T_{\rm sfc}$ is the surface temperature. The net solar radiative flux is allowed to penetrate the surface and be absorbed within the ice (Grenfell 1979). The amount of penetration depends on the snow cover, the cloud fraction, and the depth in the ice. When snow is present, virtually all of the net solar flux is absorbed within the snow; when it is absent, about 65% passes through the first ice layer and about 50% passes through the top 25 cm of ice. During the summer, the penetrating solar flux causes much of the ice melt to occur below the surface. The snow depth and the snow density are prescribed based on observations from the NP stations.

The sensible heat flux is determined by the difference between the model-calculated surface temperature and the measured 2-m air temperature using a stability-dependent exchange coefficient (Hack et al. 1993):

$$F_s = \rho c_p C_s U_{2\rm m}(T_{2\rm m} - T_{\rm sfc}), \tag{8}$$

where ρ and c_p are the air density and heat capacity, $U_{2\rm m}$ is the wind speed at a height of 2 m, and $T_{2\rm m}$ is the air temperature at a height of 2 m; C_s is the heat transfer coefficient and is a function of the bulk Richardson Number of the surface layer. A value of $C_s = 0.0023$ is used for neutral stratification. The latent heat is determined with the model-calculated surface mixing ratio $q_{\rm sfc}$ and the mixing ratio determined from the measurements of relative humidity at a height of 2 m $q_{2\rm m}$:

$$F_q = \rho L C_q U_{2\rm m}(q_{2\rm m} - q_{\rm sfc}). \tag{9}$$

In computing the latent heat flux, the latent heat of evaporation of the surface L includes the latent heat of melting if the surface temperature is below freezing. As in the CCM2 model, the transfer coefficients for heat and moisture are the same, $C_q = C_s$.

The heat storage is determined from the time rate of change in the layer temperature:

$$S_i = \Delta z_i \rho c_p \frac{\partial T_i}{\partial t}, \tag{10}$$

where ρ is the ice or snow density, c_p the heat capacity, and Δz_i the layer thickness. The total heat storage S in (1) is the sum of the S_i values. The energy available for melting is determined at each time step if a layer temperature exceeds the melting point:

$$M_i = \Delta z_i \rho c_p \frac{(T_{m,i} - T_i)}{\Delta t}, \tag{11}$$

where $T_{m,i}$ is the salinity-dependent melting point of the layer. The energy available for melting M in (1) is the sum of the M_i values.

The salinity of the ice is modeled with a fixed salinity profile that drops linearly from 3 ppt at the bottom to 0 ppt at the top. This is in rough agreement with the idealized salinity profiles for multiyear ice shown by Maykut (1985). With this salinity profile, the other physical properties of the ice can be computed as follows. The specific heat capacity is from a theoretical expression derived by Ono (1967),

$$c_{p,\rm ice} = c_0 + a(T - 273.16) + \frac{bS}{(T - 273.16)^2}, \tag{12}$$

where $c_0 = 2113$ J °C^{-1} kg^{-1}, $a = 7.53$ J °C^{-2} kg^{-1}, and $b = 18\,000$ J °C kg^{-1}. The temperature T is in kelvins and salinity S is in parts per thousand. The effective heat capacity is a strong function of the salinity and the temperature near the melting point because of the latent heat of freezing associated with brine pockets within the ice. Until the melting point is reached, the solar heat entering the ice remains as latent heat in the brine pockets. After the melting point is reached in this model, the heat available for melting M is assumed to drain away and need not be removed to begin the cooling of the ice. However, the large heat capacity near the freezing point due to the retention of liquid water in brine pockets requires the removal of a large amount of heat in the fall before substantial cooling begins. The fractional volume of brine is a strong function of temperature and salinity (Maykut 1985), rising to 15% at a temperature of -0.5°C and a salinity of 1.5 ppt (the average salinity of the ice in the model). The total melt, averaging 0.66 m of ice, is about 22% of the imposed 3-m ice thickness. Thus, the water retained within brine pockets is somewhat less than that melted after the freezing point is reached.

The melting temperature is determined from the following expression by Ono (1967):

$$T_m = 273.16 - 0.05411S, \tag{13}$$

where T is again in kelvins. The specific heat in snow is taken from Anderson (1976). It is similar to that of pure ice, which also exhibits a strong dependence on temperature due to its crystalline structure:

$$c_{p,\rm snow} = 92.88 + 7.364T. \tag{14}$$

The heat conduction at the interface between layers i and $i + 1$ is proportional to the vertical temperature gradient:

$$F_{c,i} = k_j(T_{i+1} - T_i)/\Delta z_j, \tag{15}$$

where T_i is the layer temperature, Δz_j is the distance between the centers of layers i and $i + 1$, and k_j is the average thermal conductivity of the two layers. The thermal conductivity of ice is from an expression proposed by Untersteiner (1961):

$$k_{\rm ice} = k_0 + \frac{\beta S}{(T - 273.16)} \tag{16}$$

in which $k_0 = 2.2$ W m^{-1} K^{-1} and $\beta = 0.13$ W m^{-1}. The conductivity for snow is from Ebert and Curry (1993) and includes the temperature-dependent effects of vapor diffusion:

$$k_{\rm snow} = 2.845 \times 10^{-6}\rho^2 + 2.7 \times 10^{-4}\, 2.0^{(T-233)/5}, \tag{17}$$

where the temperature T of the snow is in kelvins and

the snow density ρ is taken from observations at each ice camp.

The bottom flux F_B in (1) is the conductive flux in the lowest layer. The temperature of the bottom of the ice is assumed to be a constant -1.8°C. Consequently, in the winter, there is a substantial heat flux from the bottom surface. In the model, the thickness of the ice does not change, but this flux could be considered to come both from the ocean and from the latent heat of freezing at the bottom surface. A freezing rate could be determined if a value were assumed for the oceanic heat flux. In the summer, the ice temperature rises to the melting point, which, because of the low salinity of the ice, is warmer than the ocean temperature, so the bottom heat flux reverses sign.

The surface energy balance model and thermodynamic ice model have been checked with eddy-correlation measurements of the sensible heat flux made at the LeadEx ice camp in the Beaufort Sea in the spring of 1992. The surface turbulence measurements are reported by Ruffieux et al. (1995) who estimate an error of ± 2 W m^{-2} in the measured sensible heat flux. The model was forced with the measured wind speed, air temperature, humidity, and downwelling long- and shortwave radiative fluxes. The measured sensible heat flux had a mean of 2.9 W m^{-2} and a standard deviation of 10.5 W m^{-2}. The mean difference between the sensible heat flux estimated by the model and that measured during LeadEx was -1.8 W m^{-2}, and the rms difference was 6.2 W m^{-2}. A full description of the intercomparison is given by Lindsay et al. (1997).

c. One year at one station

We begin our discussion of the results by showing the forcing parameters and resultant fluxes for just one station: NP-30 in 1990. Figure 3 shows the smoothed time-dependent forcing parameters obtained for this station using a 10-day running-mean filter. Because of the filter, the strong diurnal cycle in the downwelling shortwave radiative flux is not apparent. The computed values of the six terms of the energy balance equation, (1), also smoothed with a 10-day filter, are shown in Fig. 4. Note the relatively short time period in which significant energy is available for melting and the large amount of heat stored in the ice near day 190 (10 July). A time-versus-depth cross section of the ice temperature is shown in Fig. 5. The ice temperature cross section is similar to what MU71 found in their model study using monthly mean values. Note the lag in the cooling of the ice near the bottom until the early winter; this lag is caused by the considerable heat capacity of the ice–brine matrix.

3. Temporal variability

a. Annual cycle of the energy balance

The entire 45 yr are combined to define the seasonal cycle of the energy balance. Box plots are used to show the median, the quartiles, and the 5th and 95th percentiles of the 3-h values of each parameter by month. Figure 6 shows the annual cycles of the principal forcing parameters and Fig. 7 shows the annual cycles of the terms of the energy balance equation, (1). The variation illustrated by the box plots includes short-term (within the month), interannual, and spatial variability. The seasonal cycles are similar to what has been found by others, but it is noteworthy that there is considerable variation, as indicated by the box plots, in both the forcings and the fluxes.

Table 1 shows the monthly mean values and the standard deviations of the monthly means for each of the principal forcing parameters and the terms of the energy balance equation (1). Here, the standard deviations represent spatial and interannual variability of the monthly mean values and, as a consequence, represent much less variability than exhibited in the 3-h values used to construct the box plots in Figs. 6 and 7. All of the forcing parameters show seasonal cycles consistent with previous climatologies. Note, however, the large variability in most of them. Of particular impact on the energy balance is the variability in the albedo. The albedo is smallest in July, averaging 0.65; at some stations it remains high all summer, never dropping below 0.80. At these stations some snow remained on the ice surface all summer, or there was significant snowfall during the summer.

The monthly mean values of the downwelling radiative fluxes, the albedo, the net radiation, and the turbulent fluxes are compared in Fig. 8 with those used by M82 (for 3-m thick ice) and Ebert and Curry (1993). The Ebert and Curry results for net radiation and turbulent fluxes are area averages (including leads), so they are not comparable to our results for nonponded ice and are not included in the figure. The area-averaged flux values depend critically on the imposed lead concentration. The M82 study used prescribed values for the downwelling radiative fluxes and the turbulent fluxes. The monthly averaged radiative fluxes were from Marshunova (1961) and are based on data from the NP stations, so the good agreement with our values is to be expected. The turbulent fluxes were based on estimates made by Doronin (1963), whereas this study computes the turbulent fluxes based on the measured air temperatures and the modeled ice-surface temperatures. In general, our computed flux values are similar to those used by M82, although the sensible heat fluxes show some significant differences in both the winter and the summer.

The net radiation is remarkably constant through the winter months, averaging about -27 W m^{-2}. It changes from negative to positive in May, with the largest positive flux in July, not June when the solstice occurs, because of the lower albedo in July. The net radiation changes to negative again in September. The sensible heat flux is positive in the winter, about 7–10 W m^{-2}, and is negative only in May, when the increasing solar

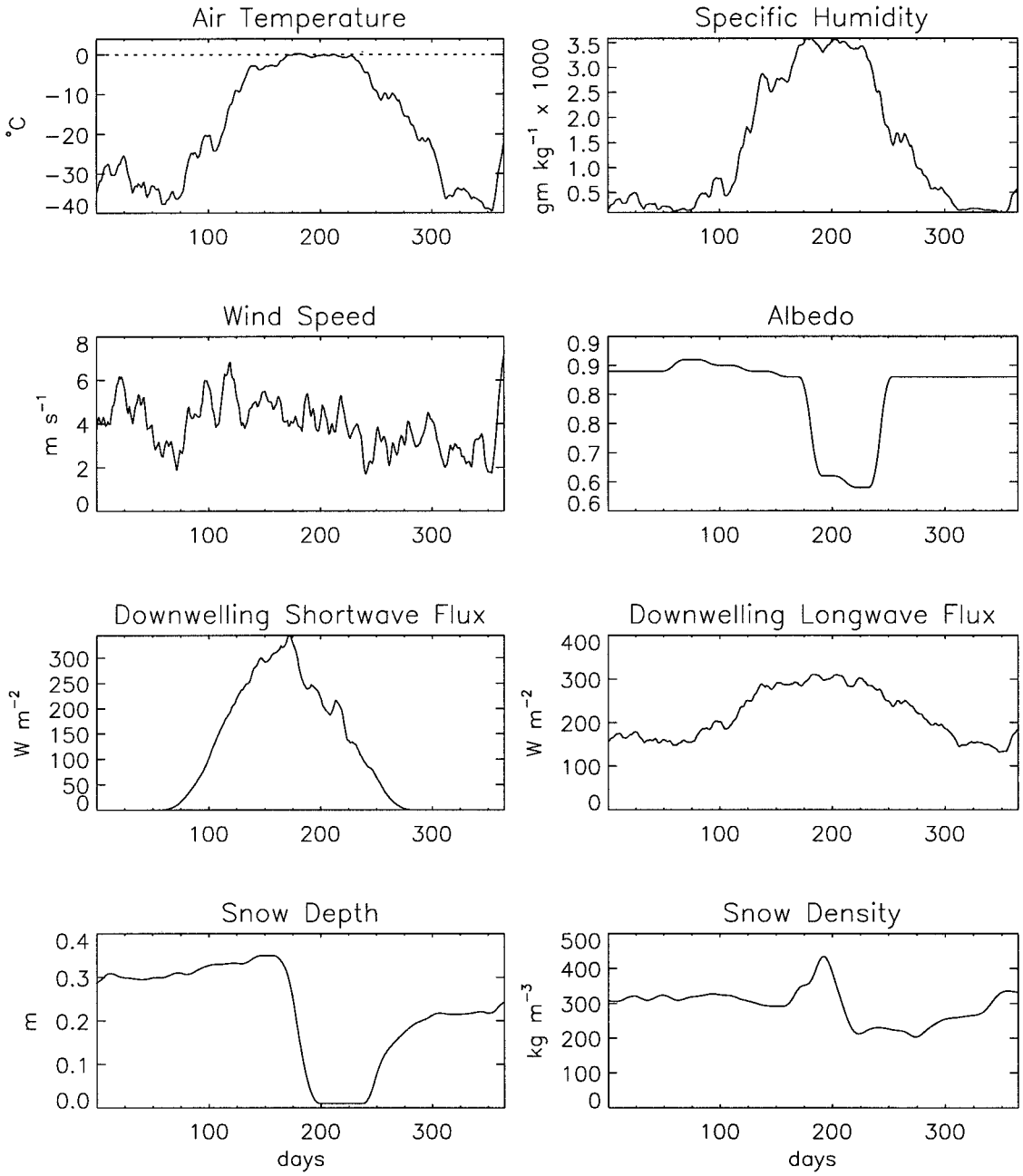

FIG. 3. Forcing parameters for NP-30 (1990) smoothed with a 10-day running-mean filter.

flux warms the surface above the air temperature. The latent heat is near zero in the winter and averages −10 W m^{-2} in June. The bottom flux is near 15 W m^{-2} in January and exhibits very little variability from station to station. In the summer, the bottom flux is negative indicating that the ice is warmer than the imposed −1.8°C bottom boundary condition. The rate of heat storage is greatest in July, when the net radiation is most positive. The ice temperature does not increase much at this time, but the specific heat is large owing to the latent heat of melting absorbed in the expanding brine pockets. The energy available for melting is maximum in July, but it has a large range, from less than 10% of the mean to over 200% of the mean. The greatest rate of cooling is in the fall, when the net radiation becomes negative. The heat stored in the ice slows the cooling of the ice substantially. The importance of the release of the stored heat in the fall, which produces a nonlinear temperature profile within the ice, was also pointed out by MU71 and Makshtas (1991).

The annual cycle of the energy balance is illustrated in Fig. 9, in which the monthly mean values of each of

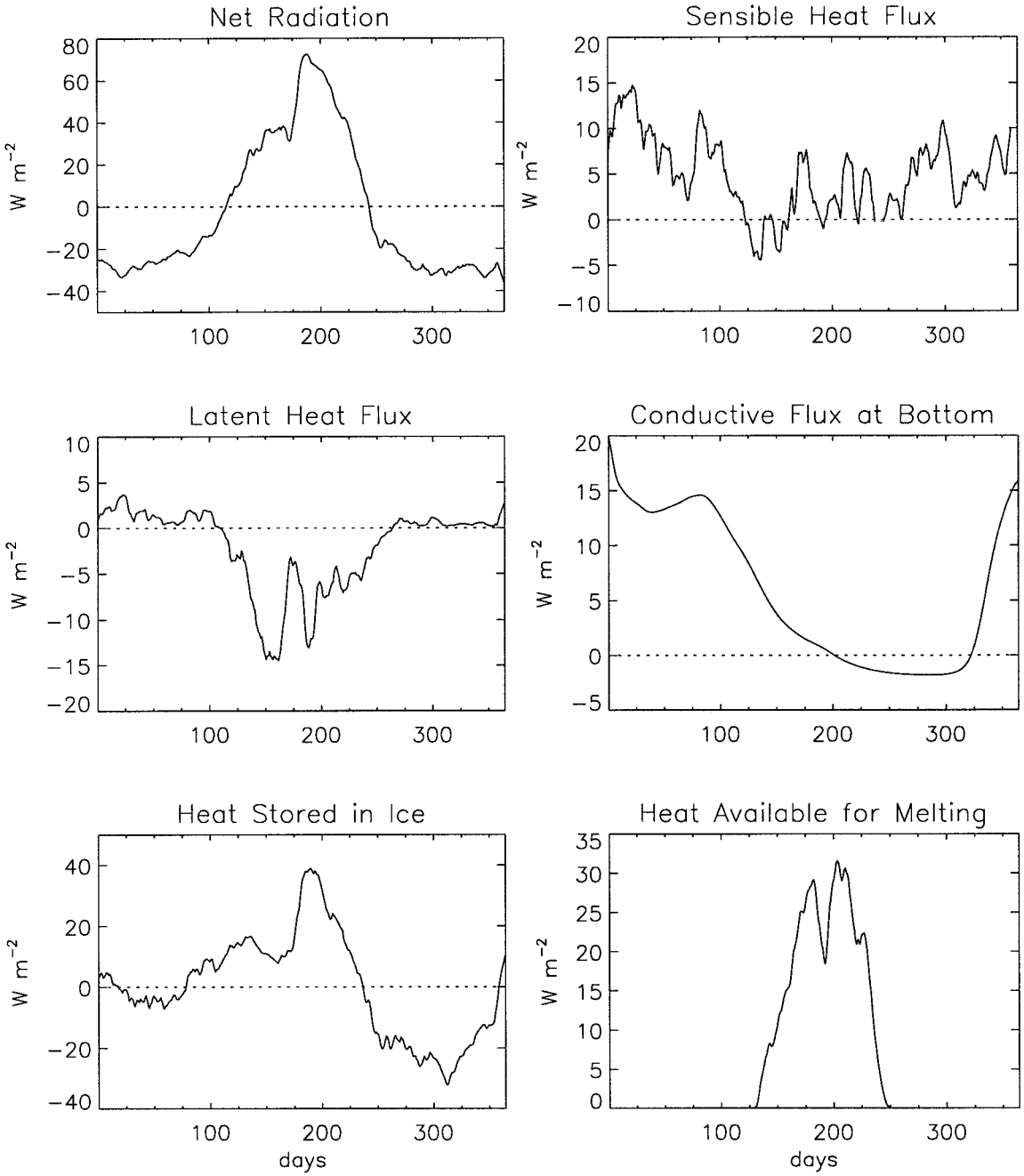

FIG. 4. The six terms of the energy balance equation computed for NP-30 (1990) and smoothed with a 10-day running-mean filter.

the terms of (1) are plotted. In the winter, the net radiative loss is balanced mostly by the bottom flux with very little heat storage or loss; however, the sensible heat flux also accounts for about a third of the net radiation. In the spring, the net radiation and the turbulent fluxes become small, and the conductive flux from the ocean begins to warm the ice. In the summer, the strong positive net radiation is largely balanced by storage and melt (in nearly equal parts) and, to a lesser extent, by the surface latent heat flux. Finally, in the fall, the net radiation again becomes negative, and it is balanced mostly by a cooling of the ice (the storage term). The turbulent fluxes and the bottom flux are all small.

Note that the annual average net radiation is just 0.5 W m^{-2}, which is remarkably close to zero, since there is nothing in the procedures that would force such a close balance. Small changes in the downwelling radiative fluxes or in the surface albedo could change the net radiation significantly. The annual average heat storage is also small, just 0.3 W m^{-2}, well within the un-

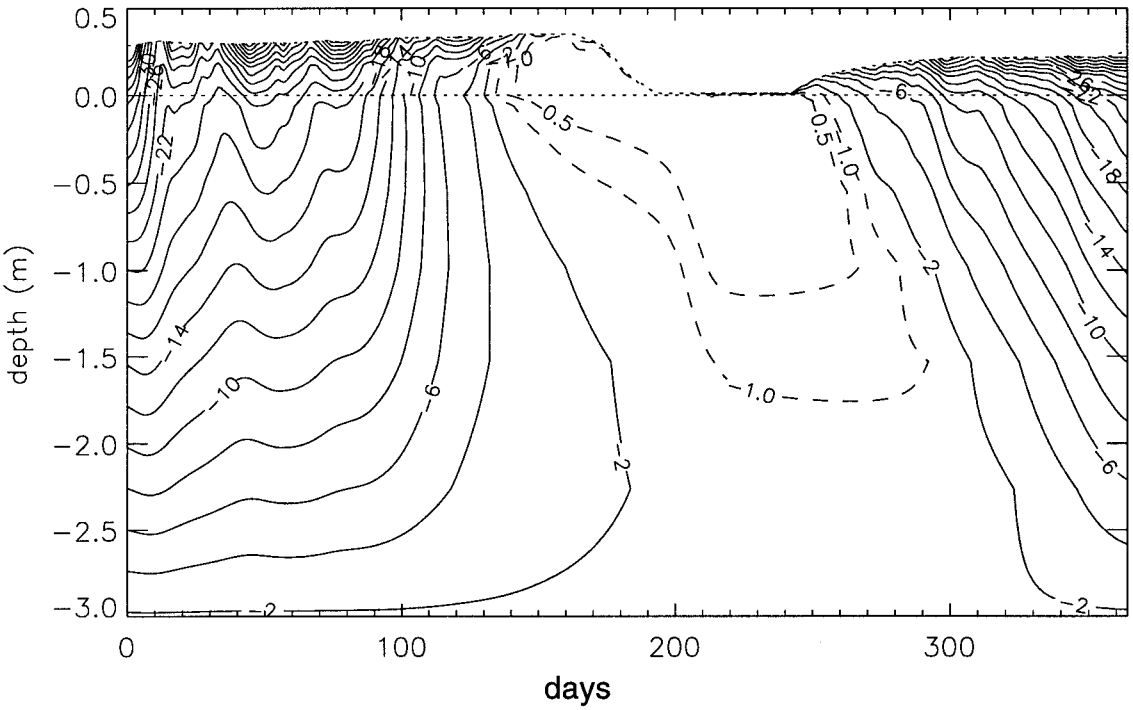

FIG. 5. Cross section of the ice temperature versus time and depth for NP-30 (1990) in degrees Celsius. The dotted lines show the top of the snow and the top of the ice. The field has been smoothed with a 10-day running-mean filter.

certainty of the net radiation. Because we are modeling only one small part of the whole system and do not include lead processes or melt ponds, we need not expect an equilibrium energy balance to ensure a stable ice cover.

This dataset offers an opportunity to quantify the well-known dependence of the air temperature on the wind speed and cloud cover. Table 2 shows the monthly mean air temperatures, the standard deviations of the 3-h observations, and the squared correlation coefficients R^2 for total cloud amount and wind speed. The wind or clouds during the winter individually account for 20%–30% of the within-month variance. A linear model for the air temperature that includes both the cloud fraction and the wind speed is

$$T_{2m} = a_0 + a_c c + a_w U_{2m} + \varepsilon, \qquad (18)$$

where a_0 is the intercept, a_c and a_w are the coefficients for cloud fraction and wind speed, and ε is the error. As shown in Table 2, this model accounts for about 40% of the winter within-month air temperature variance. The difference between cloud-free and cloud-covered conditions is greatest in October, when overcast skies are accompanied by temperatures 10.4°C warmer than found with clear skies. The difference between windy and calm conditions is greatest in December, when a wind of 10 m s^{-1} is accompanied by temperatures averaging 11.1°C warmer than those found under calm conditions. In the summer, there is no significant relationship between the air temperature and the cloud cover or the wind speed. This linear model might offer a simple correction for estimating the surface temperatures under clouds based on satellite observations of the nearby clear-sky surface temperatures.

b. *Short-term variability of forcings and fluxes: 3 h to 16 days*

The scale-dependent variability of the forcings and fluxes on timescales of 3 h to 16 days is analyzed with the formalism of the discrete orthogonal wavelet transform. This method offers a simple and direct determination of the variability associated with each temporal scale and of the times that the variability occurs. It is particularly well suited for analyzing nonstationary time series, such as the annual cycle of the various parameters under study here. There are numerous references in the literature to the use of the wavelet transform in geophysical analysis. The techniques used here are outlined by Lindsay et al. (1996).

The discrete wavelet transform is based on the application of a sequence of high-pass and low-pass filters, in this case a Haar wavelet filter of length 2. The Haar wavelet coefficients are lagged differences of running-mean smooths of the series and are identical to the Allen variance used in many applications. The maximal-overlap algorithm, introduced by Percival and Guttorp (1994), is used to determine the wavelet variance. This algorithm determines the coefficients, one for each scale, for every step in the time series and offers a more

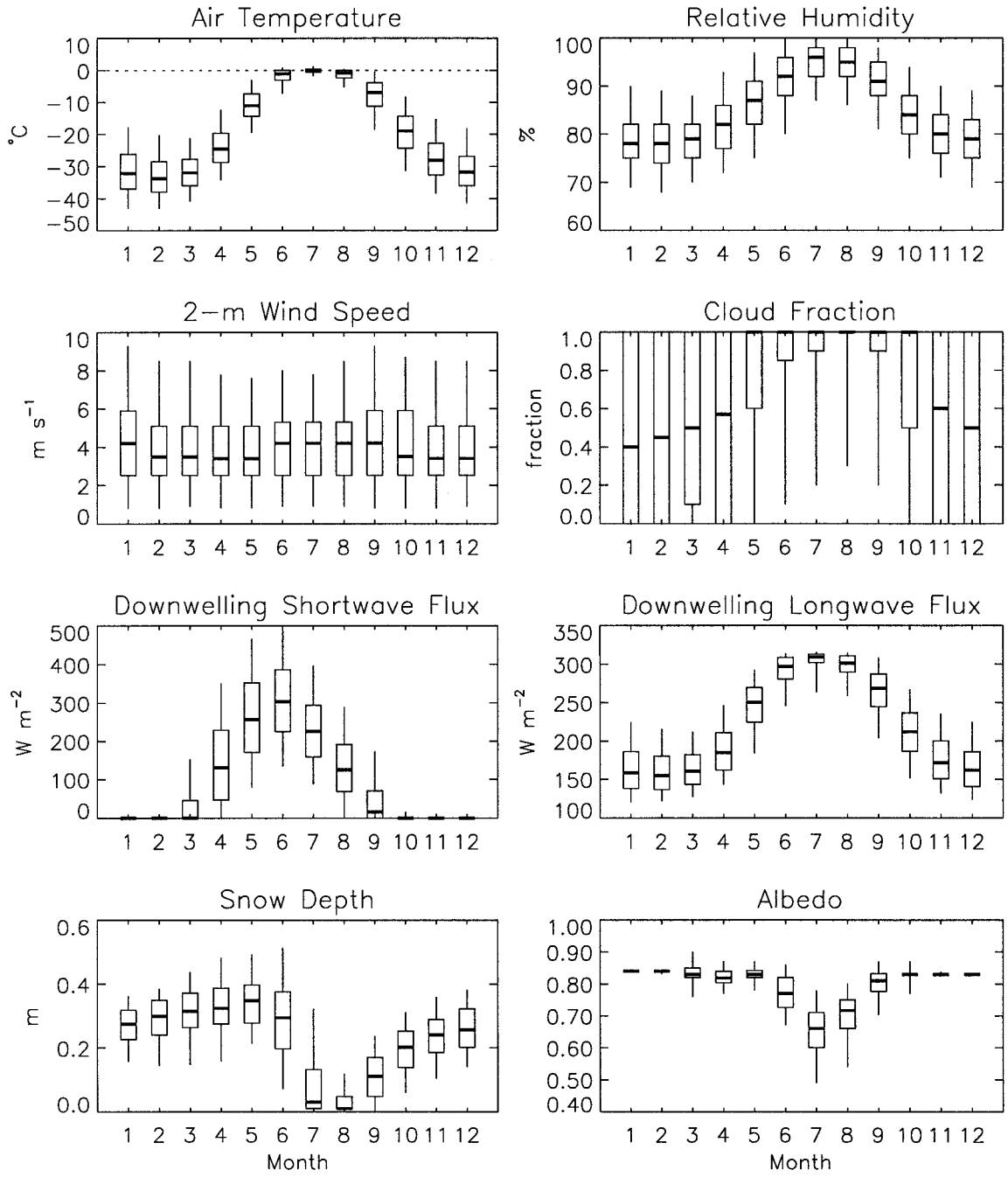

FIG. 6. Monthly box plots of the forcing parameters for the 45 station years. Each box plot shows the 5th, 25th, 50th, 75th, and 95th percentile values. Thus, half of the observations fall within the range indicated by the box, 90% fall within the range indicated by the vertical lines, and the median value is the horizontal line near the middle of each box. The distributions are based on 3-h values.

exact estimate of the temporal variability than the orthogonal-pyramid algorithm introduced by Mallet (1989).

Because the transform is orthogonal, the sum of the wavelet variances over all scales is equal to the variance of the observations. In this study, the wavelet coefficients are determined for eight different scales running from 3 h to 16 days. The seasonal wavelet variance is then found by summing the squares of the coefficients for each season. Note that this is a simple procedure with the wavelet decomposition, since the coefficients are localized in time, unlike the coefficients of the Fourier transform. This advantage is one of the principal reasons why the wavelet variance is used here. The plots

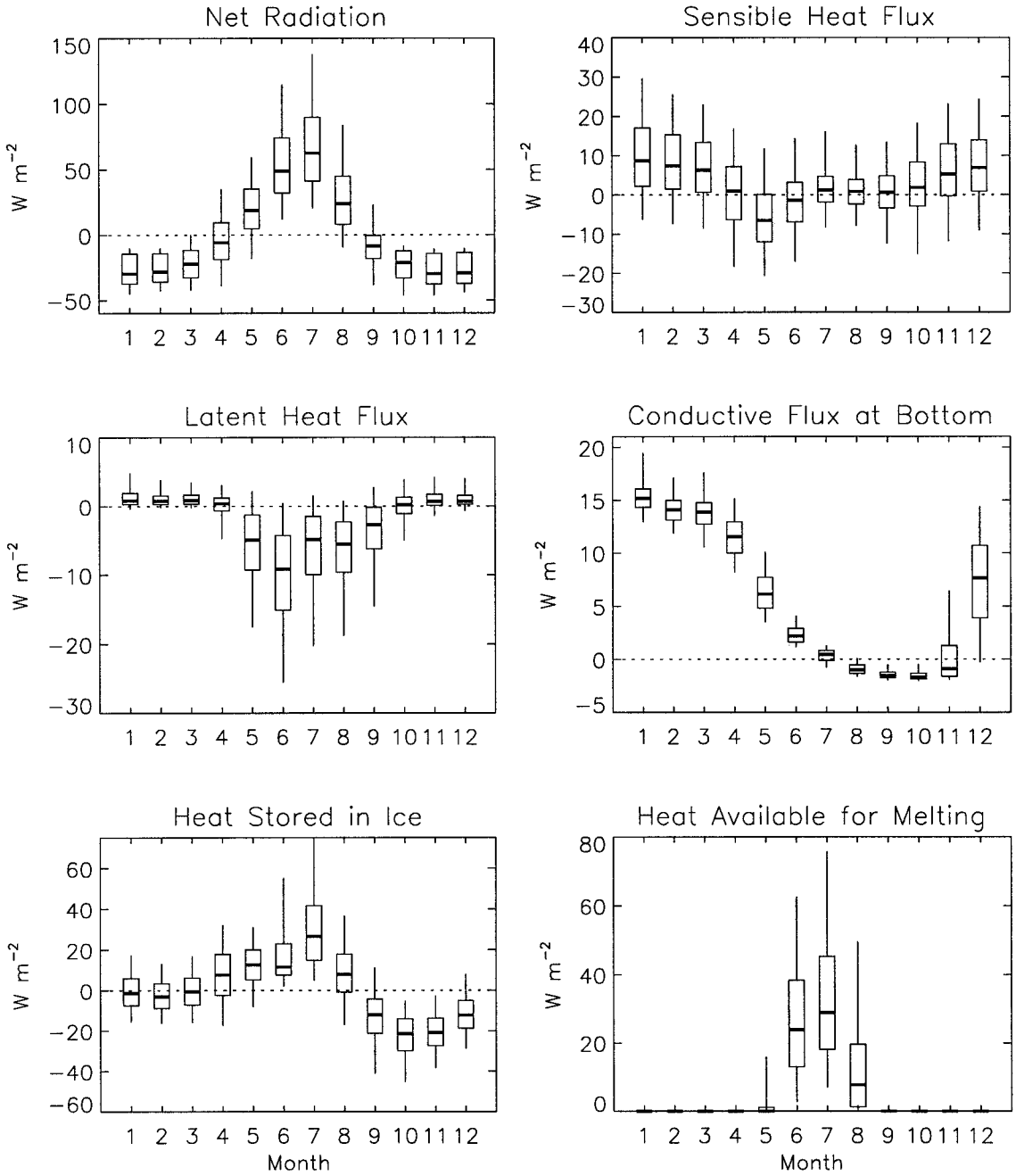

FIG. 7. Monthly box plots of the terms of the energy balance equation (1), for 45 yr of NP drifting ice-station data. The distributions are based on the 3-h calculated flux values.

shown are log-linear plots of wavelet variance versus temporal scale.

In a Fourier-centric view of the world, the Haar filters are the worst approximation of ideal high- and low-pass filters, since they are subject to severe leakage effects compared with higher-order (longer) wavelet filters (Daubechies 1992; Lindsay et al. 1996b). The lack of correspondence with a Fourier analysis is, however, balanced by an easy and direct interpretation of the wavelet variance that is calculated: it is simply the variance of the difference between adjacent nonoverlapping samples averaged over a period corresponding to the timescale.

Figure 10 shows the wavelet variance of the six forcing parameters with significant small-scale temporal variability for each of the four seasons. The downwelling shortwave flux shows the greatest variability at diurnal timescales, 6 and 12 h. The strength of the di-

TABLE 1. Monthly mean values of principal forcing parameters and energy fluxes in (1) and the standard deviations of the monthly means.

	Jan	Feb	Mar	Apr	May	Jun	Jul	Aug	Sep	Oct	Nov	Dec
Forcing parameters												
Downwelling shortwave flux (W m^{-2})												
Mean:	0.0	1.2	31.5	146.0	263.3	307.9	230.6	134.7	44.2	2.6	0.0	0.0
Std dev:	0.0	1.9	14.0	9.7	6.8	11.4	13.7	8.2	14.7	4.3	0.0	0.0
Downwelling longwave flux (W m^{-2})												
Mean:	164.0	160.5	164.1	188.1	245.2	291.2	303.9	297.0	263.8	210.9	177.0	166.0
Std dev:	13.1	13.0	9.6	12.1	11.2	6.2	3.9	5.7	11.9	12.4	13.6	9.4
2-m air temperature (C)												
Mean:	−31.4	−32.8	−31.6	−24.1	−11.0	−1.8	−0.1	−1.4	−8.0	−19.5	−27.6	−31.1
Std dev:	3.6	3.6	2.6	2.7	2.1	0.9	0.3	0.7	2.4	2.7	3.4	2.3
Relative humidity (%)												
Mean:	78.7	78.4	79.6	82.1	86.5	91.7	95.1	94.3	90.7	83.8	80.1	78.7
Std dev:	4.6	4.7	4.7	4.8	3.6	1.9	1.5	1.8	2.2	3.5	5.3	6.0
2-m wind speed (m s^{-1})												
Mean:	4.4	4.0	4.0	3.9	3.9	4.2	4.1	4.2	4.5	4.2	3.9	4.0
Std dev:	0.9	0.8	0.7	0.8	0.6	0.7	0.6	0.8	0.8	0.9	0.8	0.9
Total cloud fraction												
Mean:	0.47	0.49	0.50	0.53	0.76	0.85	0.89	0.91	0.88	0.75	0.54	0.51
Std dev:	0.13	0.14	0.13	0.11	0.09	0.09	0.07	0.07	0.05	0.10	0.12	0.12
Albedo												
Mean:			0.83	0.82	0.83	0.77	0.65	0.70	0.80	0.83		
Std dev:			0.04	0.03	0.02	0.06	0.08	0.08	0.05	0.02		
Snow depth (m)												
Mean:	0.27	0.29	0.31	0.33	0.34	0.29	0.09	0.03	0.11	0.19	0.24	0.26
Std dev:	0.06	0.08	0.08	0.09	0.09	0.11	0.09	0.04	0.06	0.07	0.07	0.08
Snow density (kg m^{-3})												
Mean:	304.1	313.5	320.3	322.2	327.0	349.7	379.3	223.9	236.3	272.6	287.8	295.7
Std dev:	21.4	20.8	24.3	26.9	22.9	12.2	2.5	1.2	14.5	30.2	33.8	31.6
Energy fluxes												
Net radiation (W m^{-2})												
Mean:	−27.4	−26.3	−21.9	−4.1	20.1	54.7	68.7	28.9	−8.1	−23.7	−27.9	−27.1
Std dev:	3.4	3.7	3.3	4.4	5.0	15.1	16.2	10.5	6.1	3.7	3.4	3.1
Sensible heat flux (W m^{-2})												
Mean:	9.9	8.4	6.6	0.1	−5.8	−1.6	2.2	1.2	0.5	2.0	5.6	7.0
Std dev:	3.6	3.6	3.3	3.3	3.0	2.6	2.6	1.7	2.1	3.2	3.8	3.1
Latent heat flux (W m^{-2})												
Mean:	1.3	1.1	1.1	−0.0	−5.9	−10.3	−6.5	−6.7	−3.9	−0.1	1.0	1.1
Std dev:	0.8	0.6	0.5	0.9	1.7	2.7	3.5	2.6	2.1	0.9	0.9	0.8
Bottom flux (W m^{-2})												
Mean:	15.4	14.2	13.9	11.6	6.4	2.3	0.4	−0.9	−1.5	−1.5	0.4	7.4
Std dev:	0.7	1.4	1.9	1.8	1.2	0.5	0.4	0.5	0.4	0.5	2.4	3.8
Heat storage (W m^{-2})												
Mean:	−0.8	−2.6	−0.3	7.5	12.2	17.9	30.8	8.6	−13.5	−23.3	−20.9	−11.7
Std dev:	2.0	2.5	1.8	2.2	1.8	7.8	9.7	4.7	4.1	3.8	3.9	4.5
Energy available for melting (W m^{-2})												
Mean:	0.0	0.0	0.0	0.0	2.6	27.2	33.9	13.8	0.5	0.0	0.0	0.0
Std dev:	0.0	0.0	0.0	0.0	2.0	9.0	10.5	8.4	1.7	0.0	0.0	0.0

urnal cycle is a strong function of latitude. The variance at a scale of 12 h drops from about 2500 (W m^{-2})^2 at 75° to nearly zero at the pole. The downwelling longwave radiative flux shows the greatest variability at scales of about 2 days, but there is little variability in the summer owing to the constant cloud cover and constant temperatures. The variability increases at a scale of 16 days, because the variability associated with the annual cycle begins to be included. The air temperature shows the greatest variability in the winter at timescales

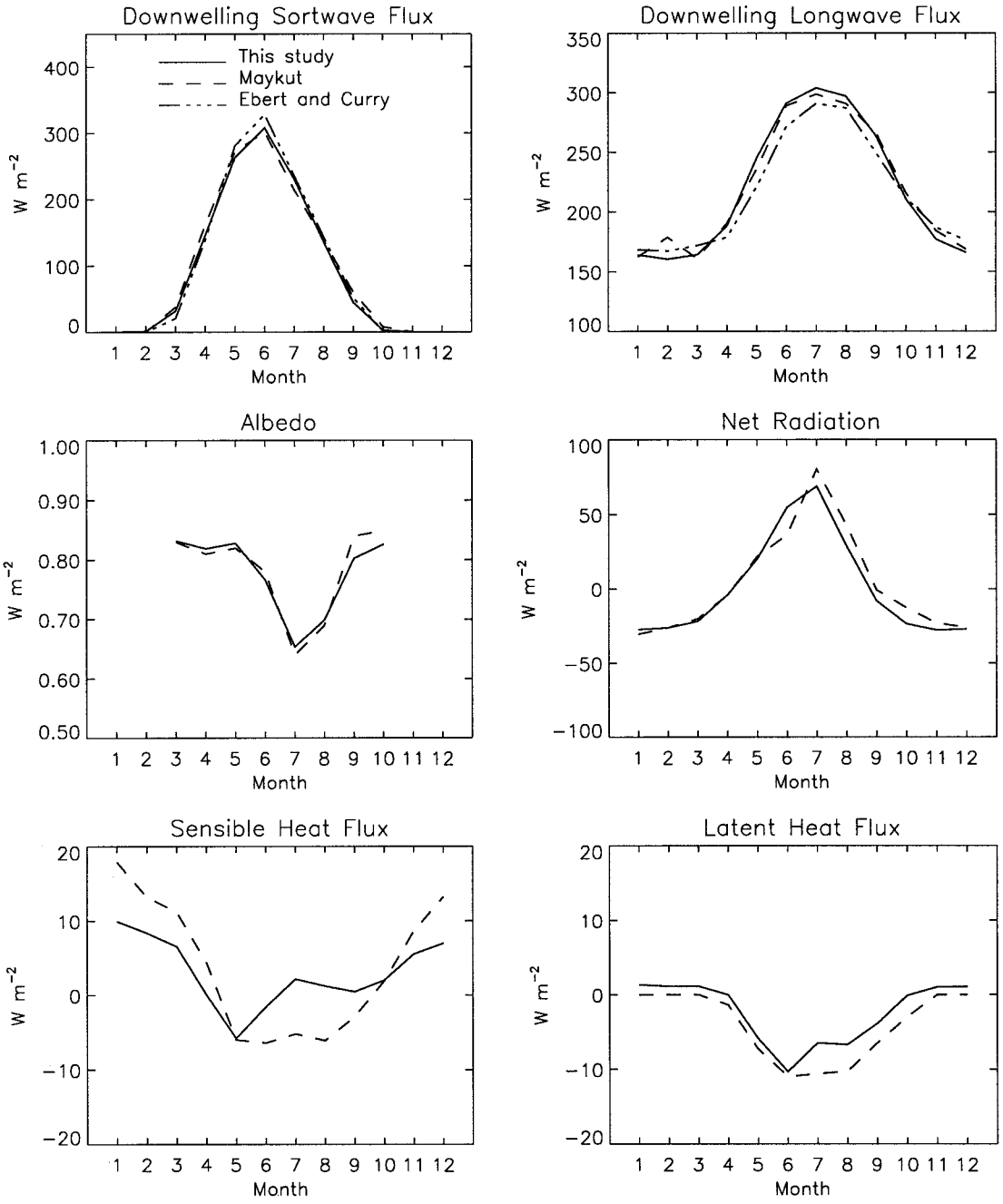

FIG. 8. Comparison of the fluxes calculated in this study with those used by Maykut (1982) for 3-m thick ice and with the downwelling radiative fluxes used by Ebert and Curry (1993).

of 8 days and little variability in the summer. The specific humidity shows the greatest variability at timescales greater than 1 day. In both the air temperature and the specific humidity, there is no clear gap between the synoptic-scale variability of several days and the annual-cycle variability that begins to be seen at a scale of 16 days. The downwelling shortwave flux and the cloud fraction exhibit such a gap. The wind speed shows peak variability at timescales of 2 days and more variability in the fall and winter than in the spring and summer. Finally, the cloud fraction, which modulates the downwelling radiation, shows the greatest variability in the winter and spring at timescales of about 1 day.

Figure 11 shows the wavelet variance of the six terms of the energy balance equation (1). The net radiation shows a strong diurnal cycle in the spring and summer, but the variability is relatively smaller in the spring because the surface albedo is high. The

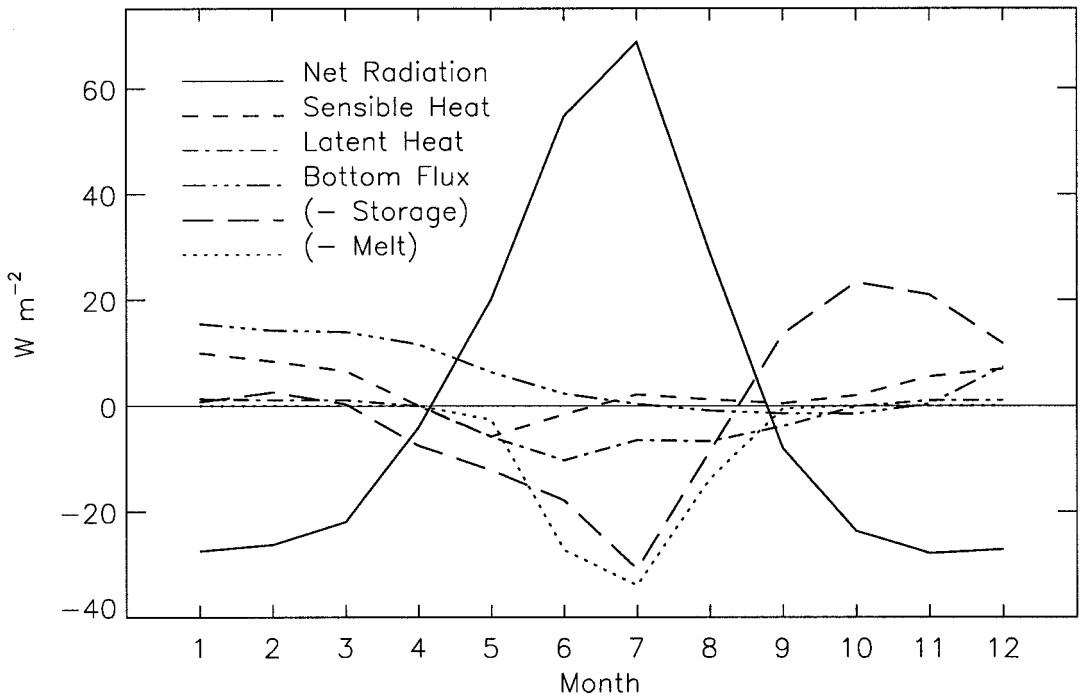

FIG. 9. Annual cycle of the energy balance. Plotted are the monthly mean values of each of the terms of (1). Their sum is zero.

sensible heat flux is most variable at the shortest timescales. The latent heat flux shows significant variability only at small scales in the summer and exhibits a weak diurnal cycle. The bottom flux shows no short-term variability and only a small amount at scales near 10 days, and mostly in the winter. Again, this variability is related to the annual cycle. The variability in heat storage is greatest in the spring and summer and also shows a diurnal cycle. Finally, the energy available for melting shows variability only in the summer and exhibits a strong diurnal cycle. Note that there is no pronounced diurnal cycle in the air temperature (Fig. 10) or the sensible heat flux (Fig. 11) in any season. The large diurnal cycle in net radiation is largely balanced by diurnal cycles in the storage and melt terms.

c. Interannual variability

There is considerable variability in the forcing parameters from year to year and from station to station, and this is reflected in the energy available for melting F_m. In Fig. 12, the total annual energy available for melting (the time integral of F_m), expressed as meters of ice, is shown for each of the 45 station years. The latent heat of freezing of pure ice is used as a conversion factor. The total annual melt averages 0.67 m of ice, ranges between 0.29 and 1.09 m, and exhibits large variations from year to year.

The interannual variability was investigated by first considering each parameter in the dataset as the sum of two elements: a high-frequency ''detail'' signal (a high-pass filtered version of the time series) and a low-fre-

TABLE 2. Air temperature related to 3-h clouds and wind speed. For definitions of a_0, a_c, and a_w see (18).

	Jan	Feb	Mar	Apr	May	Jun	Jul	Aug	Sep	Oct	Nov	Dec
Mean T_{2m} (°C)	−31.4	−32.8	−31.6	−24.1	−11.0	−1.8	−0.1	−1.4	−8.0	−19.5	−27.6	−31.1
Std dev	7.9	7.1	6.1	6.6	5.0	2.6	0.9	1.9	5.5	7.0	7.0	7.1
R^2, clouds	0.28	0.25	0.17	0.16	0.21	0.00	0.01	0.03	0.18	0.32	0.30	0.30
R^2, wind	0.23	0.20	0.20	0.14	0.05	0.02	0.00	0.00	0.07	0.13	0.19	0.24
a_0 (°C)	−39.9	−40.8	−38.2	−30.3	−16.9	−2.8	0.2	−3.0	−17.6	−30.4	−36.2	−39.3
a_c (°C)	8.0	7.3	5.1	5.2	5.8	0.4	−0.4	1.6	8.7	10.4	8.3	7.5
a_w (°C m^{-1} s)	1.08	1.09	1.03	0.90	0.39	0.16	0.03	0.01	0.43	0.76	1.03	1.11
Rms error (°C)	6.1	5.6	5.1	5.8	4.4	2.5	0.9	1.9	4.9	5.5	5.4	5.4
R^2, both	0.40	0.37	0.30	0.24	0.23	0.02	0.02	0.03	0.22	0.39	0.42	0.42

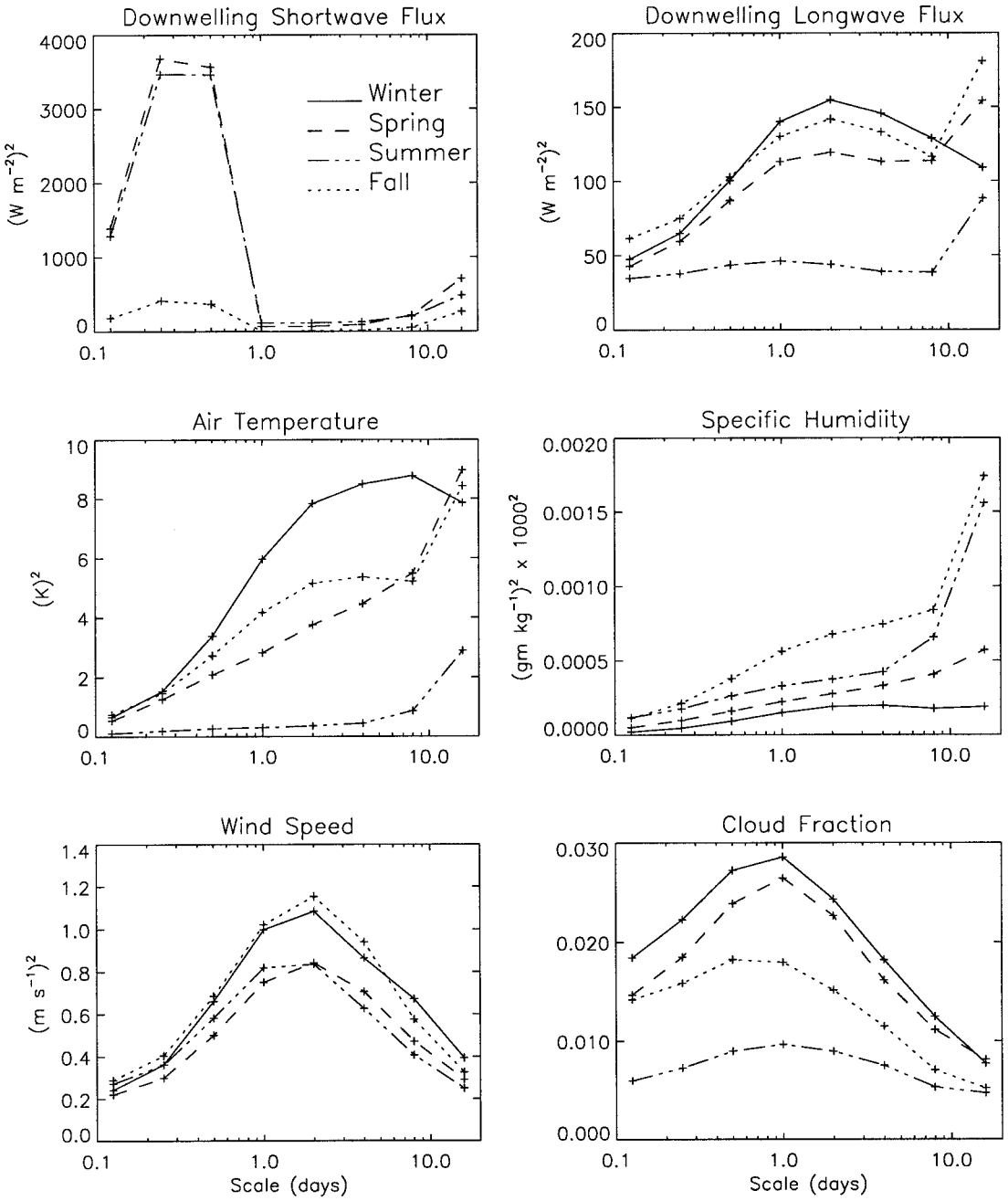

FIG. 10. Average wavelet variance of the forcing parameters with significant small-scale temporal variability. These are seasonal averages for 45 station years: winter (December–February), spring (March–May), summer (June–August), and fall (September–November). For this analysis, the Haar wavelet filter is used in the discrete wavelet transform, so that the variance at a given scale is the variance of the difference between adjacent nonoverlapping averages taken over a time period indicated by the scale. At a scale of 1 day, the downwelling shortwave flux variance is 0, 65, 113, and 3 $(\text{W m}^{-2})^2$ for winter, spring, summer, and fall.

quency 16-day smooth (a low-pass filtered version) (Lindsay et al. 1996b). The variability of the detail signal is analyzed in the previous section; here only the seasonal, spatial, and interannual variability of the smooth is considered. The smooth used here is simply the 16-day running mean.

For station k at time i, the smooth $\Psi_{i,k}$ of a parameter is modeled as the sum of a time-dependent mean seasonal cycle over all of the stations $\overline{S}_i$, plus a spatial component $X_{i,k}$, and a residual $r_{i,k}$:

$$\Psi_{i,k} = S_i + X_{i,k} + r_{i,k}. \tag{19}$$

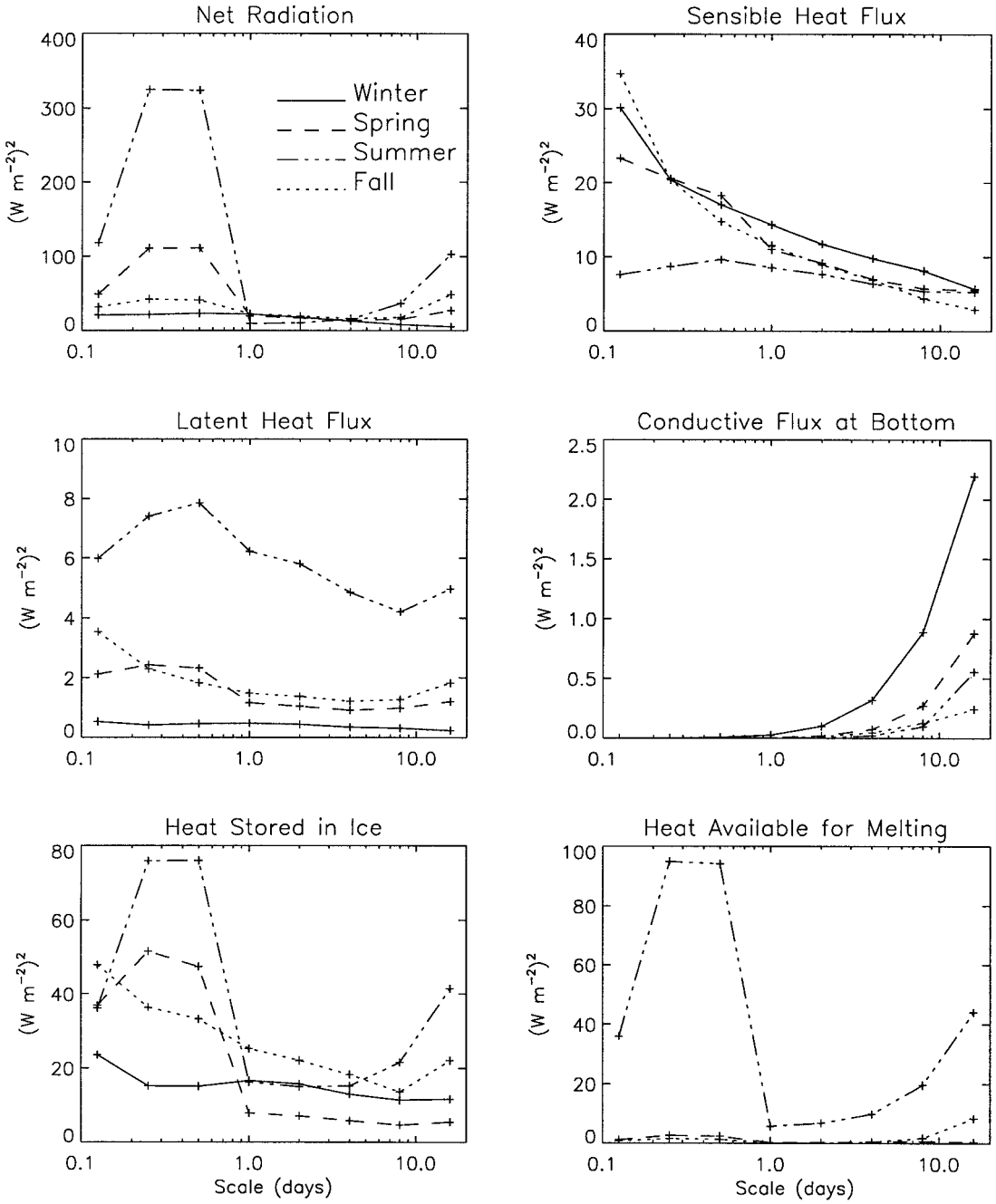

FIG. 11. Average wavelet variance of the terms of the energy balance equation for each season. At a scale of 1 day, the net radiation variance is 22, 20, 9, and 22 $(\mathrm{W\ m^{-2}})^2$ for winter, spring, summer, and fall.

The spatial component $X_{i,k}$ is modeled with a simple least squares fit to the latitude ϕ:

$$X_{i,k} = a_0 + a_1\phi_{i,k}, \tag{20}$$

where the fit is made to the difference $\Psi_{i,k} - \overline{S}_i$, and the residual of the fit is $r_{i,k}$. The limited spatial coverage of our dataset precludes more complex spatial modeling. The number of degrees of freedom is reduced in each fit because of the serial correlation of the smoothed signals (Wilks 1995). As a result, only a few of the spatial fits are significant at the 95% probability level. Increasing the complexity of the spatial fit to include, for example, a two-parameter plane component reduces the significance levels of the fits. Assuming the three contributions to the variance of Ψ are independent, the variance of the smooth can be expressed as

$$\sigma_\Psi^2 = \sigma_S^2 + \sigma_X^2 + \sigma_r^2, \tag{21}$$

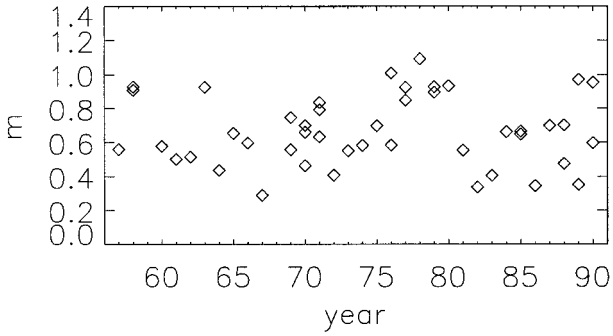

FIG. 12. Total energy available for melting expressed in terms of meters of ice that would have been ablated versus year.

in which σ_S^2 is the variance of the mean seasonal cycle, σ_X^2 is the spatial variance, and σ_r^2 is the residual interannual and unmodeled spatial variance. The variability and spatial structure of the parameters may change with the seasons, so a separate analysis is performed for each of the four seasons independently. In each season, five samples from each station were taken 16 days apart to give 225 points for each fit.

The results of this analysis for the energy fluxes are presented in Table 3, which shows the standard deviations of the total variance of the low-pass smooths along with the standard deviations of the mean seasonal cycle within the season, the mean spatial component, and the residual. Also shown are the fractions of the total low-pass variance accounted for by the mean seasonal cycle, the spatial fit, and the residual. By and large, there is little dependence on latitude in the 16-day smoothed signals. The interannual and unmodeled spatial variance accounts for over 10 W m^{-2} of the net radiation only in the summer.

4. Comments and conclusions

The air temperature is closely coupled to the surface temperature through the sensible heat flux. The air–surface temperature difference, $\Delta T = T_{2m} - T_{sfc}$, determines that flux as shown in (8). The magnitude of this difference is important in estimating the near-surface air temperature from satellite measurements of the surface temperature (Yu et al. 1995). The snow-surface temperature is determined as a free parameter in the model,

TABLE 3. Partition of variance for 16-day smoothed signals.

	Standard deviation				Fraction of total variance		
	Total	Seasonal	Spatial	Residual	Seasonal	Spatial	Residual
Net radiation							
Winter	14.4	13.7	0.9	4.2	0.92	0.00	0.08
Spring	15.1	14.4	1.3	4.4	0.91	0.01	0.09
Summer	20.1	13.4	6.6	13.6	0.45	0.11	0.46
Fall	10.7	9.3	1.8*	4.9	0.75	0.03	0.21
Sensible heat flux							
Winter	6.2	4.8	0.3	3.9	0.60	0.00	0.40
Spring	5.9	4.6	1.1	3.6	0.62	0.03	0.36
Summer	3.8	2.3	0.8	2.9	0.39	0.05	0.58
Fall	3.8	1.9	0.6	3.2	0.25	0.03	0.73
Latent heat flux							
Winter	1.6	1.2	0.1	1.1	0.55	0.01	0.45
Spring	2.2	1.9	0.3	1.1	0.73	0.02	0.26
Summer	4.1	2.1	0.7	3.5	0.26	0.03	0.73
Fall	2.8	2.2	0.6	1.6	0.63	0.04	0.33
Bottom flux							
Winter	4.2	3.6	0.8*	2.0	0.74	0.04	0.22
Spring	3.1	2.6	0.6*	1.6	0.68	0.04	0.28
Summer	1.4	1.3	0.2	0.4	0.89	0.02	0.10
Fall	1.1	0.4	0.6	1.0	0.16	0.26	0.75
Heat storage							
Winter	8.6	7.7	0.8	3.8	0.80	0.01	0.20
Spring	6.0	5.5	0.6*	2.4	0.83	0.01	0.16
Summer	12.3	8.3	2.9	8.8	0.45	0.05	0.51
Fall	7.1	5.4	0.5	4.5	0.59	0.00	0.41
Energy available for melting							
Winter	0.0	0.0	0.0	0.0	0.06	0.00	0.92
Spring	0.4	0.2	0.3	0.4	0.21	0.75	0.79
Summer	12.3	6.8	4.2	9.5	0.31	0.12	0.60
Fall	1.5	0.4	0.3*	1.4	0.07	0.05	0.88

* Indicates significant spatial fit at the 95% confidence level.

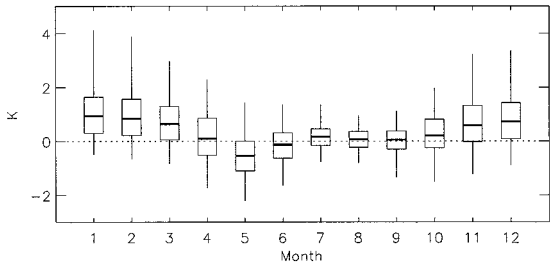

FIG. 13. Monthly box plots of the 3-h modeled air–surface temperature difference $\Delta T = T_{2m} - T_{sfc}$, where T_{2m} is the air temperature at a height of 2 m and T_{sfc} is the surface temperature.

so the statistics of the difference are easily determined. Figure 13 shows monthly box plots of the modeled ΔT values. The air is commonly stable in the winter and nearly neutral in the early spring, summer, and fall, just as we saw for the sensible heat flux. Only in May, when the rate of surface warming is greatest, is ΔT significantly negative, and there is an upward sensible heat flux as seen in Fig. 7. During the summer, the surface is melting and the surface temperature is maintained close to the freezing point (0°C) so that the temperature difference is largely established by the measured air temperature. In all months, the mean value is closely related to the wind speed. In January, for example, the mean value of ΔT is 2.0 K for winds less than 2 m s^{-1} but only 0.4 K for winds greater than 10 m s^{-1}. In general, the absolute value of ΔT approaches zero with high winds, but in the summer, when near-neutral stratification is common ($\Delta T \approx 0.0$ K), the air becomes more stable with high winds, perhaps because warm air aloft is mixed down to near the surface, while the ice remains near the freezing point.

The snow-surface temperature was measured routinely at the NP drifting stations from September to April with an alcohol-in-glass thermometer placed on top of the snow. The temperature was recorded to the nearest °C. The air–surface temperature difference ΔT is found by subtracting the surface temperature from the air temperature which was measured in a Stevenson-type screen at a height of 2 m. The monthly mean values show rough agreement; however, the monthly squared correlation coefficients for the 3-h observations do not rise above 0.15. The poor correlation could be due to inaccuracies in the model-forcing parameters (in particular, the temporal variation in the downwelling radiative fluxes) to inaccuracies in the model's physics (in particular, the thermal conductivity of the snow or the turbulent fluxes) or, finally, to inaccuracies in the measurements (in particular, the coarse resolution of the recorded snow-surface temperature). It is not possible to sort out the exact cause of the poor correlation from this dataset alone, but accurate measurements of the surface temperature without the use of a radiometer are notoriously difficult.

The date of the onset of the melt season and its length

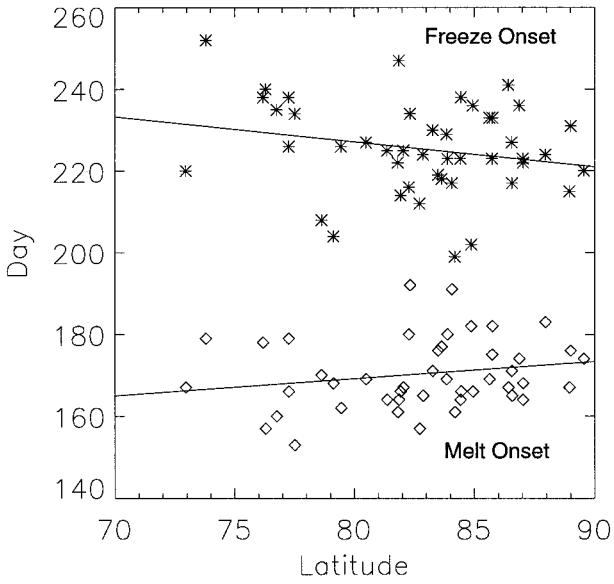

FIG. 14. Dates of the onset of melting and freezing as a function of latitude.

are often thought of as sensitive indicators of the total amount of melting to expect. The dates of the onset of melting and freezing are determined by a procedure suggested by R. Colony (1994, personal communication). The 2-m air temperature is filtered with a 2-week running-median filter, and the first and last day that the filtered temperature is above a threshold of −0.5°C are determined. For this threshold, the average date of melt onset is 19 June (day 170), with a range from 2 June to 11 July (days 153 to 192). The average date of freeze onset is 13 August (day 225), with a range from 18 July to 9 September (days 199 to 252). The average length of the melt season is 55 days, with a range from 20 to 83 days. There is a weak dependence of these dates on latitude, as shown in Fig. 14, with less than 5% of the variance in either of the dates being explained by latitude.

The total melt (Fig. 12) is most closely correlated with the albedo in July, June, and August (correlation coefficient $R = -0.86$, -0.73, and -0.64), the length of the melt season ($R = 0.60$), the latitude ($R = -0.54$), and the air temperature in July ($R = 0.51$). The high correlation with albedo is, of course, a manifestation of the well-known ice/albedo feedback. Note that the length of the melt season is more important in explaining the total ice melt ($R = 0.64$) than when the melt season begins ($R = -0.32$) or ends ($R = 0.49$). Our use of albedo values appropriate for nonponded ice means that over entire floes, which have a lower average albedo in the summer, there would be more total melt. In this dataset there is about 0.21 m more melt for each 0.10 decrease in the July albedo.

The freezing rate can be determined from the conductive flux at the bottom of the ice if an oceanic heat

flux is assumed. This heat flux is assumed to be zero, and the monthly freezing rate is determined by converting the average monthly bottom flux to the equivalent change in ice thickness; this conversion is done using the latent heat of freezing for freshwater, as was done for the total melt. The result is an average total accretion of 0.58 m. This is a close match to the average total melt of 0.67 m, considering that there is a wide range in the ablation and accretion values found for different stations and different years. The oceanic heat flux is more likely to be slightly positive; for every watt per meter squared of annual average oceanic heat flux, the annual average bottom accretion would be reduced by 0.10 m. The freezing rate is most closely correlated with the surface temperature, because the temperature gradient through the ice determines the conductive flux at the bottom and hence the freezing rate.

There is no doubt that there are large uncertainties in some aspects of the model-forcing parameters and in the simplifications inherent in the model. Yet, the NP dataset offers a valuable opportunity to make estimates of the energy balance over many years that is not easily surpassed. The downwelling radiative fluxes are perhaps the most serious approximation in the forcing parameters, since they determine the net radiation, the largest term in the energy balance equation. Although there may be considerable error in the day-to-day values, the mean values should be much better and have been verified with the measured daily-averaged flux values from the NP stations. Little information is available with which to make better estimates of the downwelling radiative fluxes, even from satellites. Adding to the uncertainty in the downwelling radiative fluxes is the uncertainty in the albedo measurements. We have used monthly-averaged albedo values as measured at the ice camps. These measurements are for the area immediately surrounding the meteorological station and do not represent the average over the thick ice of the region, including melt ponds. If melt ponds had been included, the summer albedo would have been much lower with a consequent increase in the energy absorbed and the energy available for melting. No doubt, including melt ponds would have also considerably increased the interannual variability in the modeled total ice melt.

The treatment of meltwater and melt ponds is, perhaps, the most serious approximation in the model. We do not include the formation of melt ponds, their influence on the albedo, and the storage of latent heat that they represent. In addition, a single ice class of fixed thickness is enforced. Future work could include using the NP drifting ice-station data to determine the energy balance for different ice classes, including ponded ice as well as thin ice. These energy balance calculations, with the addition of ice-thickness distribution estimates and pond-fraction estimates, would allow a more complete determination of the regional energy balance of the ice.

The energy balance of thick ice has been computed in the past, but usually using climatological-mean forcing values. Here, the energy balance is computed using 3-h measured values of the air temperature, wind speed, humidity, cloud cover, and albedo for 45 annual cycles taken at 21 different drifting ice stations of the former Soviet Union. The mean annual cycle of the forcings and the fluxes, their short-term variability, monthly variability, and interannual variability have all been determined. The determination of the variability in the forcings and the fluxes over thick ice will help in the design of observational programs that seek to monitor the state and evolution of the Arctic ice pack.

Acknowledgments. I would like to acknowledge fruitful discussions with G. Maykut and R. Colony and the helpful comments of the reviewers. This work was generously supported by Office of Naval Research Grant N000-14-96-10070 and National Aeronautics and Space Administration Grant NAGW 4950.

REFERENCES

Anderson, E. A., 1976: A point energy and mass balance model of a snow cover. NOAA Tech. Rep. NWS 19, NOAA, Washington, DC, 150 pp.

Daubechies, I., 1992: *Ten Lectures on Wavelets.* Society for Industrial and Applied Mathematics, 357 pp.

Doronin, Y. P., 1963: On the heat balance in the central Arctic (in Russian). *Proc. Arctic Antarctic Res. Inst.,* **253,** 178–184.

Ebert, E. E., and J. A. Curry, 1993: An intermediate one-dimensional thermodynamic sea ice model for investigating ice–atmosphere interactions. *J. Geophys. Res.,* **98,** 10 085–10 109.

Efimova, N. A., 1961: On methods of calculating monthly values of net long-wave radiation. *Meteor. Gidrol.,* **10,** 28–33.

Grenfell, T. C., 1979: The effects of ice thickness on the exchange of solar radiation over the polar oceans. *J. Glaciol.,* **22,** 305–320.

Guest, P. S., and K. L. Davidson, 1994: Factors affecting variations of snow surface temperature and air temperature over sea ice in winter. *The Polar Oceans and Their Role in Shaping the Global Environment, Geophys. Monogr.,* No. 85, Amer. Geophys. Union, 435–442.

Hack, J. J., B. A. Boville, B. P. Brieglib, J. T. Kiehl, P. J. Rasch, and D. L. Williamson, 1993: Description of the NCAR Community Climate Model (CCM2). NCAR Tech. Note TN-382+STR, NCAR, Boulder, CO, 108 pp.

Jacobs, J. D., 1978: Radiation climate of Broughton Island. *Energy Budget Studies in Relation to Fast-Ice Breakup Processes in Davis Strait,* R. G. and J. D. Jacobs, Eds., INSTAAR, University of Colorado, 105–120.

Key, J. R., R. A. Silcox, and R. S. Stone, 1996: Evaluation of surface radiative flux parameterizations for use in sea ice models. *J. Geophys. Res.,* **101,** 3839–3849.

Lindsay, R. W., D. B. Percival, and D. A. Rothrock, 1996: The discrete wavelet transform and the scale analysis of the surface properties of sea ice. *IEEE Trans. Geosci. Remote Sens.,* **34,** 771–787.

——, J. A. Francis, P. O. G. Persson, D. A. Rothrock, and A. J. Schweiger, 1997: Surface turbulent fluxes over pack ice inferred from TOVS observations. *Ann. Glaciol.,* **25,** 393–399.

Makshtas, A. P., 1991: *The Heat Budget of Arctic Ice in the Winter.* International Glaciological Society, 77 pp.

Mallat, S., 1989: A theory for multiresolution signal decomposition: The wavelet representation. *IEEE Trans. Pattern Anal. Mach. Intell.,* **11,** 674–693.

Marshunova, M. S., 1961: Principal characteristics of the radiation balance of the underlying surface and of the atmosphere in the

Arctic (in Russian). *Proc. Arctic Antarctic Res. Inst.,* **229,** 5–53.

——, and A. A. Mishin, 1994: *Handbook of the Radiation Regime of the Arctic Basin* (*Results from the Drifting Stations*). Applied Physics Laboratory, University of Washington, 69 pp.

Maykut, G. A., 1982: Large-scale heat exchange and ice production in the central Arctic. *J. Geophys. Res.,* **87,** 7971–7984.

——, 1985: An introduction to ice in the polar oceans. APL-UW 8510, Applied Physics Laboratory, University of Washington, Seattle, WA, 107 pp.

——, and N. Untersteiner, 1971: Some results from a time-dependent thermodynamic model of sea ice. *J. Geophys. Res.,* **76,** 1550–1575.

National Snow and Ice Data Center, 1996: *Arctic Ocean Snow and Meteorological Observations from Russian Drifting Stations.* NSIDC, University of Colorado, Boulder, CO, CD-ROM. [Available from nsidc@kryos.colorado.edu.]

Ono, N., 1967: Specific heat and heat of fusion of sea ice. *Physics of Snow and Ice,* H. Oura, Ed., Institute of Low Temperature Science, 599–610.

Overland, J. E., and K. L. Davidson, 1992: Geostrophic drag coefficients over sea ice. *Tellus,* **44A,** 54–66.

Percival, D. B., and P. Guttorp, 1994: Long-memory processes, the Allan variance and wavelets. *Wavelets in Geophysics,* E. Foufoula-Georgiou and P. Kumar, Eds., Academic Press, 325–343.

Ruffieux, D., P. O. Persson, C. W. Fairall, and D. E. Wolfe, 1995: Ice pack and lead surface energy budgets during LEADEX 1992. *J. Geophys. Res.,* **100,** 4593–4612.

Schweiger, A., and J. Key, 1997: Estimating surface radiation fluxes in the Arctic from TOVS HIRS and MSU brightness temperatures. *Int. J. Remote Sens.,* **18,** 955–970.

Shine, K. P., 1984: Parameterization of the shortwave flux over high albedo surfaces as a function of cloud thickness and surface albedo. *Quart. J. Roy. Meteor. Soc.,* **110,** 747–764.

Untersteiner, N., 1961: On the mass and heat budget of Arctic sea ice. *Arch. Meteor. Geophys. Bioklimatol.,* **A12,** 151–182.

Wilks, D. S., 1995: *Statistical Methods in the Atmospheric Sciences.* Academic Press, 467 pp.

Yu, Y., D. A. Rothrock, and R. W. Lindsay, 1995: Accuracy of sea ice temperature derived from the advanced very high resolution radiometer. *J. Geophys. Res.,* **100,** 4525–4532.